CHEMISTRY OF MATERIALS
Cite This: Chem. Mater. 2018, 30, 6377−6388
Article
pubs.acs.org/cm

# Probing Surface Defects of InP Quantum Dots Using Phosphorus Kα and Kβ X-ray Emission Spectroscopy

Jennifer L. Stein,[†] William M. Holden,[‡] Amrit Venkatesh,[§,∥] M. Elizabeth Mundy,[†] Aaron J. Rossini,[§,∥] Gerald T. Seidler,*[,‡] and Brandi M. Cossairt*[,†]

[†]Department of Chemistry, University of Washington, Seattle, Washington 98195-1700, United States
[‡]Department of Physics, University of Washington, Seattle, Washington 98195-1560, United States
[§]Department of Chemistry, Iowa State University, Ames, Iowa 50011, United States
[∥]U.S. Department of Energy Ames Laboratory, Ames, Iowa 50011, United States

Supporting Information

**ABSTRACT:** Synthetic efforts to prepare indium phosphide (InP) quantum dots (QDs) have historically generated emissive materials with lower than unity quantum yields. This property has been attributed to structural and electronic defects associated with the InP core as well as the chemistry of the shell materials used to overcoat and passivate the InP surface. Consequently, the uniformity of the core−shell interface plays a critical role. Using X-ray emission spectroscopy (XES) performed with a recently developed benchtop spectrometer, we studied the evolution of oxidized phosphorus species arising across a series of common, but chemically distinct, synthetic methods for InP QD particle growth and subsequent ZnE (E = S or Se) shell deposition. XES afforded us the ability to measure the speciation of phosphorus reliably, quantitatively, and more efficiently (with respect to both the quantity of material required and the speed of the measurement) than with traditional techniques, i.e., X-ray photoelectron spectroscopy and magic angle spinning solid state nuclear magnetic resonance spectroscopy. Our findings indicate that even with deliberate care to prevent phosphorus oxidation during InP core synthesis, typical shelling approaches unintentionally introduce oxidative defects at the core−shell interface, limiting the attainable photoluminescence quantum yields.

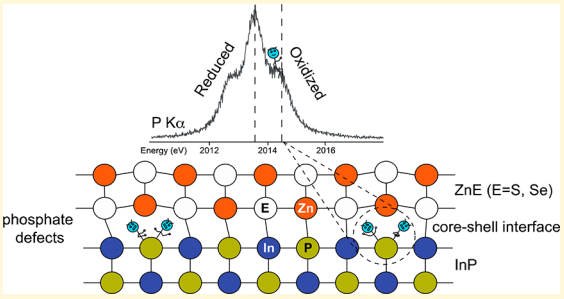


## INTRODUCTION

Indium phosphide (InP) quantum dots (QDs) are the leading cadmium-free emissive material for luminescence down-conversion applications, such as LED-backlit displays, and lighting technologies.[1−5] Display manufacturers, including Samsung, Sony, Vizio, LG, and Apple, have devoted significant resources to investigating methods for narrowing the size distributions of InP QD samples and increasing the photoluminescence quantum yields (PL QYs) to 100%.[6] Despite these efforts, state-of-the-art syntheses produce QD ensembles that are characterized by luminescence line widths in the green and red region that range between 40 and 80 nm and maximum quantum yields of 85% in the most sophisticated shelled samples.[7−9] While minimizing defects in the core and shell materials is necessary, perhaps the most crucial aspect of design is at the core−shell interface. InP QDs have been shown to be incredibly susceptible to surface oxidation from *in situ* and *ex situ* sources during both core and shell syntheses, resulting in oxidized phosphorus species that likely perturb conformal shell growth.[10−12] We hypothesize that surface phosphorus oxidation plays a leading role in limiting our ability to access higher-quality samples.

Even under synthetic conditions in which extreme care is taken to exclude oxygen and water, surface phosphorus oxidation often arises as the result of undesired side reactions that occur during the nucleation, growth, and shelling of InP QDs. Although there has been debate concerning the potential benefits of an amorphous oxidized interface between an InP core and its shell material with respect to reducing lattice strain between materials,[13,14] the detrimental impact of water on particle nucleation and growth has directed efforts toward removing any source of surface oxidation.[15−17] Furthermore, oxidized phosphorus that is present at the core−shell interface may serve as an electronic trap site or prevent conformal deposition of shell material, both of which have the effect of reducing PL QYs. In this study, we chose three different synthetic methods that are expected to produce InP QDs with minimal or no oxidation. Furthermore, each InP QD was shelled with either ZnS or ZnSe with the hypothesis that samples that are initially more oxidized or subjected to

Received: June 19, 2018
Revised: August 31, 2018
Published: August 31, 2018





DOI: 10.1021/acs.chemmater.8b02590
Chem. Mater. 2018, 30, 6377−6388

processes that oxidize the surface will result in particles with lower PL QYs.

X-ray photoelectron spectroscopy (XPS) and magic angle spinning solid state nuclear magnetic resonance (MAS SSNMR) spectroscopy have been the traditional routes for measuring the degree of oxidized phosphorus present in InP QDs.[11−13,17−19] These measurements can be challenging because of the low sensitivity of SSNMR spectroscopy, which traditionally requires large amounts of sample and long acquisition times. XPS analysis is generally impeded by its surface-sensitive nature and the presence of common long-chain surface ligands that further limit the escape depth of the photogenerated electrons and reduce the signal resolution.[20] Extremely high-energy resolution wavelength dispersive X-ray fluorescence spectroscopy, more commonly called X-ray emission spectroscopy (XES), is an appealing alternative method for characterizing the oxidation of phosphorus in a bulk sample because it does not face these obstacles. Recent progress in benchtop XES instrumentation holds the potential to develop XES of sulfur and phosphorus into an accessible and powerful technique for probing the oxidation state and bonding electronic structure, achieving synchrotron-level energy resolution and count rates with a spectrometer illuminated by only a conventional X-ray tube.[21] The same instrument was used in a recent study of sulfur speciation in biochars as a first analytical application,[22] and the study presented here reinforces and, in many ways, exceeds the message of that earlier work in emphasizing new potential for XES for routine application in analytical chemistry.

A number of recent studies have demonstrated the capability of synchrotron- and laboratory-based XES to measure speciation in phosphorus, sulfur, and chlorine compounds.[22−27] In particular, P K$\alpha$ XES has been used to quantitatively determine the fraction of phosphorus species with different local charge densities (i.e., oxidation states). The K$\alpha$ emission line corresponds to a transition of an electron between the deep, atomic-like 2p and 1s orbitals. In the simplest treatment, the sensitivity of this transition to changes in the valence electron population comes from the different changes in the screening of the nuclear charge as observed from the 2p and 1s orbitals. As these effects are only weakly perturbative for phosphorus (but can be much more complex for, e.g., 3d transition metals), the K$\alpha$ emission spectra typically show only a shift of the peak position from a lower to higher energy with an increasing oxidation state, while the spectral shape remains unchanged (Figure 1). For a compound containing phosphorus in multiple oxidation states, the proportion of each oxidation state can be determined quantitatively by simple linear combination fitting to multiple line shapes, although this benefits from prior knowledge of a suitable reference spectrum set.

For information beyond oxidation state determination by the P K$\alpha$ emission, P K$\beta$ XES enables a more detailed interrogation of the electronic structure. The K$\beta$ emission line results from electronic transitions from the 3p shell, suitably hybridized with valence and semicore ligand electrons, to the 1s core hole. Because of the direct relevance of such a characterization of the bonding electronic density of states for chemistry, this type of valence to core (VTC) XES is seeing growing use, such as in studies of organometallic systems.[28−31] Thus, the K$\beta$ emission has increased chemical sensitivity and can provide information about bonding, symmetry, and ligand type.[24] A full interpretation of the various spectral features

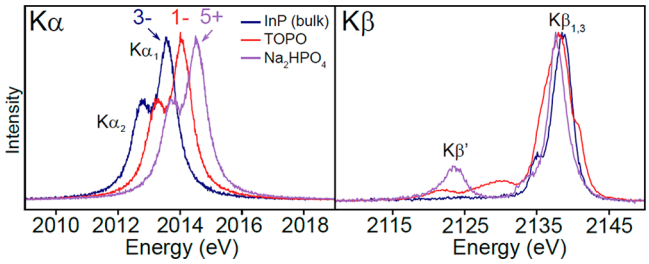


**Figure 1.** P K$\alpha$ and K$\beta$ X-ray emission spectra of reference compounds. The K$\alpha$ spectra of the three compounds are nearly identical, with shifts toward higher energies with increasing oxidation states. Nominal oxidation states of the reference compounds are indicated above the given spectra. The K$\beta$ spectra show a valence to core transition, and a number of different spectral features are observed. Of particular importance is the strong K$\beta'$ peak at 2123.5 eV in the $Na_2HPO_4$ spectra, which is due to mixing of the P 3p and O 2s orbitals and thus serves as a fingerprint of P−O bonds from the phosphate.

requires quantum chemistry calculations.[24,28,32,33] Here, we focus on the ligand fingerprinting capability of the K$\beta$ spectral features, specifically the K$\beta'$ satellite feature near 2123.5 eV in the phosphate spectrum. This feature results from mixing of P valence states with an O 2s orbital[24,34] and thus serves as a clear indicator of the presence of phosphate. P K$\beta$ spectra are shown for reference compounds in Figure 1.

## EXPERIMENTAL SECTION

**X-ray Emission Spectroscopy.** P K$\alpha$ and K$\beta$ XES measurements were performed on a recently developed laboratory spectrometer, described in detail by Holden et al.[21] The spectrometer uses a low-power, unfocused X-ray tube (Varex VF50, 50 W) to illuminate the sample, whose emitted X-rays are analyzed by a 10 cm radius of curvature cylindrical crystal analyzer and detected using a new homemade CMOS direct-exposure color X-ray camera.[21,35] The spectrometer makes use of the dispersive refocusing Rowland (DRR) geometry, in which the sample is placed within the Rowland circle and illuminated with an unfocused beam of incident radiation while a position-sensitive detector is placed tangential to the circle at the location of the refocused fluorescence. This method of illumination allows efficient collection of the signal from the sample, and the entire energy region of interest is measured simultaneously by the CMOS camera functioning as a position-sensitive detector with sufficient single-photon energy resolution to reject background scatter and chamber-wall fluorescence. The wavelength dispersing component is a Si(111) cylindrically bent Johann analyzer having a 10 cm radius of curvature (XRSTech). The Si(111) analyzer provides Bragg angles of 79° for P K$\alpha$ (~2014 eV) and 67.6° for P K$\beta$ (~2138 eV). To prevent air contamination during XES measurements, the sample and crystal are inside a small vacuum chamber that was pumped to a pressure of <100 mTorr during the measurements. For improved resolution at P K$\alpha$, the crystal analyzer was masked using aluminum foil to a 10 mm × 2 mm region (along Rowland plane × out of Rowland plane). For the weaker P K$\beta$ signal, the crystal was unmasked to improve count rates at the expense of an increased Johann error. The Johann error causes weak tails on the high-energy side of the spectrum. These distortions do not significantly affect the analysis of the P K$\beta$ spectra used here. The energy scale of P K$\alpha$ and K$\beta$ measurements is calculated on the basis of the instrumental geometry with $Na_2HPO_4$ as a reference standard having K$\alpha_1$ and K$\beta_{1,3}$ energy positions at 2014.55 and 2137.80 eV, respectively.[24]

The InP QD samples were prepared for XES measurements by being drop-cast onto silicon wafers with a spot size ~3−4 mm in diameter with <5 mg of material. The drop-cast samples were stored in an inert nitrogen atmosphere and briefly exposed to air while being loaded into the instrument. The wafers were mounted in the


DOI: 10.1021/acs.chemmater.8b02590
Chem. Mater. 2018, 30, 6377−6388

instrument, and the drop-cast spot was exposed directly to the incident beam. With the current instrumental configuration, switching between K$\alpha$ and K$\beta$ measurements requires manually repositioning the crystal analyzer and retuning; thus, the measurements were done in batches to separately measure K$\alpha$ and K$\beta$. Fresh InP QD samples were drop-cast for each measurement.

The P K$\alpha$ emission spectra were analyzed using linear combination fitting with the nonlinear least-squares fitting Python package LMFIT.[36] With a few exceptions discussed below, spectra were fit with two oxidation state components, each consisting of two Voigt profiles representing the spin-split K$\alpha_1$/K$\alpha_2$ peaks. The widths and height ratios of these peak shapes were constrained to the values obtained from fitting the bulk InP and $Na_2HPO_4$ reference compounds, and the energy positions of the two peak shapes were allowed to vary. The fits were weighted assuming Poisson statistics. The speciation was calculated from the relative intensity of the fit components.

The primary source of systematic uncertainty in this approach is due to limited prior knowledge of the number of distinct oxidation states in the sample. For the InP QDs, our primary expectation is a superposition of a low-energy K$\alpha_{1,2}$ spin−orbit split doublet representing the reduced phosphorus in the InP cores and a higher-energy K$\alpha_{1,2}$ doublet due to surface-oxidized phosphorus species. If an appreciable amount of a third phosphorus species exists in an oxidation state between these two extremes, the energy positions and results of the phosphide-versus-phosphate speciation based on the erroneous two-component fit will be skewed. As discussed in the Results and Discussion, this effect was observed for samples where TOP-Se was used as a precursor, producing TOPO as a byproduct. To analyze the spectra for those samples, linear combination fitting was performed with three components, where the energy positions of the reduced and oxidized components were allowed to vary, but the TOPO component was fixed to be at 2014.07 eV, as determined by measurement of a pure reference TOPO sample.

Another source of systematic uncertainty is variations in the detailed shape of the K$\alpha_{1,2}$ doublet for the components of the fitting procedure. Though these variations have not been reported in detail for phosphorus, variations in the K$\alpha_{1,2}$ intensity ratio in the range of 1.7−2.3 have been reported for a variety of sulfur compounds.[25] In addition, variations in the Voigt widths of the line shapes on the order of 2% are observed for the reference compounds measured here. The effects of these variations on the systematic uncertainty were estimated by performing the fitting procedure over a range of intensity ratios and widths, and the results are given in Tables S1 and S2.

During the P K$\alpha$ measurements, changes in speciation due to possible radiation damage were checked by performing the speciation calculations on subsets of the accumulated data. The results are shown in Figures S1 and S2. The majority of the samples changed speciation by less than ±2% during the measurements and vary nonmonotonically. For the three samples that show large monotonic changes, **C**-InP, **C**/ZnS, and InP/Zn, it is believed that a vacuum leak may have contributed. For those samples, only the first scan was kept for the final results. The vacuum leak was addressed before the remaining samples were measured.

To obtain a final estimate of the uncertainty from the XES fitting results, the uncertainty from signal variation over time was combined with the uncertainties estimated by varying the K$\alpha_{1,2}$ intensity ratio and Voigt widths and added to the statistical uncertainty. The full details are listed in Table S1 and S2, and the final uncertainty estimates are listed in Table 1.

**$^{31}$P MAS SSNMR Spectroscopy.** All quantum dot samples were prepared for SSNMR analysis from concentrated colloidal solutions (~50 mg of dried QDs in 1 mL of anhydrous toluene) by impregnating 150−450 $\mu$L of the colloidal solutions in 8−12 mg of boron nitride, in 50 $\mu$L aliquots. The mixture was allowed to dry on a watch glass for 1 h before being packed into a 1.3 mm rotor. To confirm that there is a minimal increase in the level of oxidation induced by this procedure, $^{31}$P SSNMR spectra were obtained from InP QDs after being exposed to air for 10 days (Figure S3). These tests indicated that there should be minimal oxidation over the course of several hours that are required to prepare the samples for SSNMR experiments.

**Table 1. Comparison of SSNMR and P K$\alpha$ XES for Determination of the Phosphorus Oxidation State in InP QDs**

| sample | SSNMR (% red) | SSNMR (% ox) | P K$\alpha$ XES (% red) | P K$\alpha$ XES (% ox) |
|---|---|---|---|---|
| InP | 93 | 7 | 89 ± 3 | 11 ± 3 |
| InP/Zn | 87 | 13 | 83 ± 4 | 17 ± 4 |
| InP/ZnS | 54 | 46 | 51 ± 5 | 49 ± 5 |

MAS $^{31}$P SSNMR spectra were recorded using a Bruker Avance III HD console on a wide-bore 9.4 T magnet [$\nu_0(^{31}P)$ = 162.1 MHz]. All experiments were performed using a 1.3 mm fast MAS broadband HX SSNMR probe, and the rotors were spun with nitrogen gas to prevent additional oxidation of the QDs during the course of the measurements. $^{31}$P MAS NMR spectra were obtained using a rotor-synchronized Hahn echo (90°−$\tau$−180°−$\tau$−acquire) pulse sequence with continuous wave $^1$H heteronuclear decoupling applied during acquisition. The pulse widths for 90° and 180° pulses were 1.3 and 2.6 $\mu$s, respectively (192 kHz RF field), and the rotor-synchronized $\tau$ periods were set such that the total echo delay was two rotor cycles. The MAS frequency was 50 kHz in all cases. Fast MAS helps to provide quantitative NMR spectra by eliminating spinning sidebands and focusing the signal into the isotropic peaks. The $^1$H RF power for continuous wave heteronuclear decoupling was set to the HORROR condition [$\nu_1(^1H)$ = 25 kHz]. All $^{31}$P SSNMR spectra were acquired with a 500 s recycle delay to ensure there was an adequate relaxation delay of $\geq 3T_1$ to give quantitative SSNMR spectra. This was confirmed by acquiring a $^{31}$P SSNMR spectrum of **C**-InP QDs with a 750 s recycle delay, which showed a comparable intensity for the phosphide signal. The spectral width was set to 200 kHz, and the number of digitized points to 8K, corresponding to a total acquisition time of 20.48 ms. $^{31}$P spectra were acquired in steps of 32 scans (4.4 h experiment time), and multiple spectra were acquired until the sum of all spectra provided a spectrum with a reasonable signal-to-noise ratio. Each spectrum was processed by zero filling up to 8K real data points and by adding a simple exponential window function with 1000 Hz line broadening. All data processing was performed with Topspin 3.5.

**X-ray Photoelectron Spectroscopy.** All XPS spectra were taken on a Surface Science Instruments S-Probe photoelectron spectrometer. This instrument has a monochromatized Al K$\alpha$ X-ray source that was operated at 20 mA and 10 kV and a low-energy electron flood gun for charge neutralization. The X-ray analysis area for these acquisitions was approximately 800 $\mu$m across. The pressure in the analytical chamber during spectral acquisition was $<5 \times 10^{-9}$ Torr. All included figures are high-resolution spectra. The pass energy for high-resolution spectra was 50 eV, and the data point spacing was 0.065 eV/step. The takeoff angle (the angle between the sample normal and the input axis of the energy analyzer) was 0°. Service Physics Hawk version 7 data analysis software was used to fit high-resolution spectra. The binding energy scale was calibrated from hydrocarbon ligands using the C 1s peak at 284.6 eV. $P_{2p}$ peaks were analyzed using a linear background, and fits were constrained with a 0.84 eV splitting value.

All InP samples were drop-cast as solutions on a Si wafer, or solids were brushed onto a strip of double-sided tape on a Si wafer. Samples were prepared in a nitrogen glovebox and transported in sealed containers to the instrument, but transfer into the instrument chamber did require a minor degree of exposure to air and/or moisture.

**General Nanoparticle Characterization.** Ultraviolet−visible (UV−vis) spectra were collected on a Cary 5000 spectrophotometer from Agilent. Fluorescence and absolute quantum yield measurements were taken on a Horiba Jobin Yvon FluoroMax-4 fluorescence spectrophotometer with the QuantaPhi integrating sphere accessory. QD solids were digested in 67% nitric acid overnight and diluted in



DOI: 10.1021/acs.chemmater.8b02590
Chem. Mater. 2018, 30, 6377−6388

18 MΩ water to collect ICP-OES compositional data using a PerkinElmer Optima 8300 instrument. Powder X-ray diffraction data were collected on solid films drop-cast onto a Si wafer using a Bruker D8 Discover diffractometer. Transmission electron microscopy (TEM) images were collected on a FEI Tecnai G2 F20 microscope. Samples for TEM imaging were prepared by spotting a 50/50 toluene/pentane solution of nanoparticles onto an ultrathin carbon on holey carbon support film purchased from Ted Pella. Solution NMR spectra were recorded on a 700 MHz Bruker Avance III spectrometer.

**General Synthetic Details.** All glassware was dried in a 160 °C oven overnight prior to use. All reactions, unless otherwise noted, were performed under an inert atmosphere of nitrogen using a glovebox or using standard Schlenk techniques. Myristic acid (≥99%), indium acetate (99.99%), anhydrous acetonitrile (99.8%), trioctylphosphine (97%), tris(diethylamino)phosphine (97%), indium chloride (99.999%), zinc chloride (99.999%), trioctylphosphine oxide (90%), InP (mesh pieces, 99.998%), sulfur powder (99.5% sublimed), and selenium powder (99.99%) were purchased from Sigma-Aldrich Chemical Co. and used without further purification. Diethyl zinc (95%) was purchased from Strem Chemicals and stored in a nitrogen atmosphere glovebox. Toluene purchased from Sigma-Aldrich Chemical Co. was collected from a solvent still and stored over activated 3 Å molecular sieves in a glovebox. 1-Octadecene (90%), oleylamine (70%), and squalane (96%) were purchased from Sigma-Aldrich Chemical Co. and dried by being stirred overnight with $CaH_2$, distilled, and stored over activated 3 Å molecular sieves in a glovebox. $C_6D_6$ was purchased from Cambridge Isotope Laboratories and similarly dried and stored. Bio-Beads S-X1 were purchased from Bio-Rad Laboratories and dried under vacuum before being stored in a glovebox. Omni Trace nitric acid was purchased from EMD Millipore; 18.2 MΩ water was collected from an EMD Millipore water purification system. Tris(trimethylsilyl)phosphine was prepared by modifying a literature procedure in which sodium naphthalene was used in place of Na/K alloy.[15] Zinc myristate was prepared from diethyl zinc and myristic acid using a modified literature procedure.[37]

**Synthesis of C-InP QDs.** **C**-InP QDs were prepared following a literature procedure[15] in which indium acetate (1.167 g, 4 mmol) and myristic acid (3.31 g, 14.5 mmol) were heated to 100 °C overnight under reduced pressure in 12 mL of ODE. **Caution:** *$P(SiMe_3)_3$ is a very reactive and pyrophoric source of phosphorus and should be handled with care.* $P(SiMe_3)_3$ (590 μL, 2 mmol) was measured into ODE (5 mL) and injected into the indium myristate solution at 315 °C. Particle growth was maintained at 285 °C and monitored by UV−vis spectroscopy. The reaction was halted by cooling the mixture to room temperature after growth for ∼20 min, and the ODE was removed through distillation under reduced pressure. The resulting QD paste was transferred into a glovebox for purification by being redissolved in a minimal amount of toluene and centrifuged to remove insoluble products, and then the particles were precipitated with acetonitrile. The flocculated solution was centrifuged at 7000 rpm, and the clear supernatant was discarded. After a single precipitation to remove residual ODE, the particles were dissolved in toluene and purified by gel permeation chromatography (GPC), which has been demonstrated as an effective purification technique for these types of materials.[38,39] For all following QD samples, standard purification entails the removal of high-boiling point solvents through distillation and a combination of precipitation cycles and GPC.

**Synthesis of InP/Zn QDs.** InP/Zn QDs were prepared following a literature procedure using **C**-InP QDs.[40] Briefly, zinc myristate (335 mg, 0.64 mmol) was heated to 80 °C in 5 mL of ODE until the solution was a cloudy white suspension. InP QDs (0.42 mmol of In) suspended in 5 mL of ODE were added to the suspension, and the suspension was heated to 200 °C for 3 h. Particles were purified by the standard procedure.

**Synthesis of M-InP QDs.** First, InP magic-sized clusters (MSCs) were synthesized following a modified preparation from our lab.[41] Indium acetate (5.605 g, 19.2 mmol) and myristic acid (15.9 g, 69.6 mmol) were heated neat at 100 °C under reduced pressure overnight. Dry toluene (50 mL) was added to the reaction flask at room temperature under $N_2$ the following day, after which $P(SiMe_3)_3$ (2.8 mL, 9.6 mmol) was measured into 10 mL of toluene and injected into the indium myristate solution at 100 °C. Cluster growth was complete within 1 h as indicated by the characteristic absorbance peak at 386 nm. The particles were concentrated to a minimal volume of toluene, centrifuged to remove insoluble products, and purified by GPC. Following purification, the absence of free acid was confirmed by $^1$H NMR spectroscopy and the MSCs were stored as a solid.

**M**-InP QDs were synthesized from InP MSCs through a modified procedure.[41] Myristate-capped InP MSCs (60 mg) were dissolved in 3 mL of ODE and transferred to a syringe. In a three-neck flask under $N_2$ on a Schlenk line, 12 mL of ODE was heated to 300 °C, at which point the MSCs were rapidly injected. Particle growth was held at 285 °C until it was complete (15−20 min), and then the particles were cooled to room temperature. Particles were purified by the standard procedure.

**Synthesis of A-InP QDs.** **A**-InP QDs were synthesized following a modified procedure as described by Brainis et al.[42] Indium chloride (50 mg, 0.23 mmol) and zinc chloride (150 mg, 1.1 mmol) were stirred in oleylamine (2.5 mL, 7.5 mmol) under reduced pressure at 120 °C for 1 h. The reaction mixture was placed under $N_2$, and at 180 °C, tris(diethylamino)phosphine (0.23 mL, 0.8 mmol) was injected and particle growth completed within approximately 20 min. After cooling to room temperature, particles were removed from oleylamine by precipitation with ethanol. GPC purification was performed once particles were redissolved in toluene.

**ZnS Shelling of C-, M-, and A-InP QDs.** ZnS shelling of InP QDs was performed following a modified procedure as described by Peng et al.[43] A purified solution of InP QDs (0.04 mmol indium) was dissolved in 7 mL of ODE and heated to 150 °C under an inert atmosphere. Initial solutions of InP QDs (**C**, **M**, and **A**) were standardized to each other by matching absorption at 310 nm. Stock solutions of zinc myristate (28.8 mg in 10 mL of ODE, 5.6 mM) and sulfur (22.4 mg in 10 mL of ODE, 0.07 M) were prepared and heated to 100 °C in Schlenk flasks in an oil bath. For the first monolayer, a 2.17 mL aliquot of the zinc myristate stock (0.012 mmol) was added to the InP particles at 150 °C. After 10 min, 170 μL (0.012 mmol) of the sulfur stock solution was added, and then the reaction mixture was heated at 220 °C for 30 min. The second monolayer was added in the same fashion with 2.89 mL (0.016 mmol) of zinc myristate and 230 μL (0.016 mmol) of sulfur. After 30 min at 220 °C, the reaction mixture was cooled and purified via the standard procedure.

**ZnSe Shelling of C-, M-, and A-InP QDs.** ZnSe shelling was performed following a modified procedure as described by Brainis et al.[42] A purified solution of InP QDs (0.04 mmol of indium) was dissolved in 10 mL of squalane and heated to 180 °C. Zinc myristate (100 mg, 0.192 mmol) suspended in squalane was injected, and the mixture was held at 180 °C for 20 min. Then, a stoichiometric TOP-Se solution was prepared by sonicating 1.755 g (22.2 mmol) of selenium in 10 mL of TOP (2.23 M), and 87 μL (0.192 mmol) of this stock was slowly injected into the reaction flask. After 140 min, a second addition of zinc myristate was added (300 mg, 0.576 mmol). At this point, the reaction temperature was set to 320 °C, and during heating, the second injection of TOP-Se was added dropwise (262 μL, 0.576 mmol). Particle luminescence was monitored at 320 °C, and the reaction mixture was cooled when the PL ceased to change (∼1 h). Particles were purified using the standard procedure.

## RESULTS AND DISCUSSION

To validate the use of K$\alpha$ XES as a method for determining P speciation in InP QDs, a series of three samples was used in a head-to-head comparison of oxidation state distributions inferred from P K$\alpha$ XES and from $^{31}$P MAS SSNMR. Notably, the InP and InP/ZnS samples have in part been previously characterized by Chaudret et al. via XPS and SSNMR spectroscopies with the primary conclusion that oxidation occurs during both synthesis and shell growth.[12] Here, samples including InP QDs, InP QDs that have been postsynthetically treated with zinc (InP/Zn), and InP QDs that have been


DOI: 10.1021/acs.chemmater.8b02590
Chem. Mater. 2018, 30, 6377−6388

shelled with ZnS (InP/ZnS) were studied. The results for all samples are presented in Table 1, and a comparison of the quantification of the phosphorus oxidation state by both $^{31}$P SSNMR and P K$\alpha$ X-ray emission spectroscopy for the InP/ZnS sample is shown in Figure 2. Additional spectra are

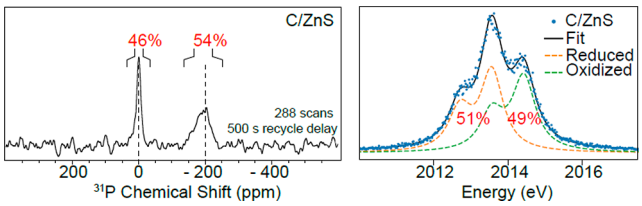


**Figure 2.** Comparison of the $^{31}$P SSNMR spectrum (left) and P K$\alpha$ XES (right) of the same batch of InP/ZnS QDs. The SSNMR signal near 0 ppm corresponds to surface phosphate, and this component appears at a K$\alpha$1 energy position of ~2014.41 eV. The relative peak areas in both types of spectra are indicated as percentages.

presented in Figure S4. Excellent agreement is found between the two techniques, and the results fall within the range of values reported by Chaudret et al.[12] The $^{31}$P SSNMR spectra generally show resonances centered at ~0 ppm, assigned to oxidized phosphate species, and −200 ppm, assigned to the core phosphide species. Cross-polarization magic angle spinning (CP-MAS) and direct excitation $^{31}$P SSNMR experiments have previously demonstrated that the oxidized phosphorus species are located at the surface of the nanocrystals.[44,45] Using the fitting procedure described in the Experimental Section, the P K$\alpha$ XES signal for each of the three samples is fit well using two oxidation state components, one with an average K$\alpha_1$ energy position of 2013.56 eV identified as InP and one higher in energy with an average position of 2014.41 eV. Although SSNMR identifies the oxidized species as phosphate-like, the K$\alpha_1$ energy position is somewhat lower than that of the disodium phosphate reference standard used (2014.55 eV). Though phosphides and sulfides are known to have small shifts in the K$\alpha_1$ energy position due to differing degrees of covalency,[24,25] this has not previously been observed in phosphates or sulfates and could be worthy of future investigation. With the identification of phosphate from the SSNMR resonance at ~0 ppm and the agreement between the SSNMR and XES results, this confirms the oxidized component at 2014.41 eV corresponds to phosphate.

These measurements demonstrate that P K$\alpha$ XES is a reliable tool for measuring phosphorus oxidation that has significant advantages over $^{31}$P SSNMR spectroscopy. Each XES measurement required <5 mg of material, and speciation could be determined within the first 30 min, though the measurements were extended to improve the resulting spectra and monitor for possible radiation damage (Figures S1 and S2). The SSNMR measurements required ~10−20 mg of material to prepare the samples for measurements (although within the 1.3 mm rotor there is likely <1 mg of material). Regardless, the SSNMR spectra typically required multiple days of collection time to obtain spectra that can be reliably integrated. On the basis of these promising data, we proceeded by measuring the extent of phosphorus oxidation as a function of the synthetic method using XES for rapid feedback, augmented by SSNMR and other methods when appropriate. Our goal was to obtain a uniquely detailed picture of the existence and origin of synthesis-specific adventitious phosphorus oxidation and its correlation with QD QY. A detailed understanding of phosphorus speciation and the degree of oxidation induced by different synthetic procedures is a critical first step in devising new synthetic routes to high-performance InP QDs.

**Surface Oxidation as a Function of Initial InP Synthesis.** Here, we evaluate the extent of oxidation that can occur in a core synthesis by studying InP QDs synthesized via three different routes. All reactions were performed under air-free conditions in a nitrogen atmosphere glovebox or on a Schlenk line. All reagents and glassware were rigorously dried as described in the Experimental Section. A summary of particle characterization for this series of InP QDs, including optical peak positions, compositions, particle sizes, and powder diffraction patterns, can be found in Table S3 and Figure S5.

The first synthesis is the most common approach for producing crystalline InP QDs through the reaction of indium carboxylates, excess carboxylic acid, and tris(trimethylsilyl)-phosphine, $P(SiMe_3)_3$, at elevated temperatures.[9,43,46] Hereafter, InP QDs prepared by this route [indium carboxylates and $P(SiMe_3)_3$] will be termed **C**-InP. Although this approach is well-established, water is generated as a byproduct from carboxylic acid ketonization at elevated temperatures, and thus, the InP QDs are detrimentally impacted through surface oxidation. This oxidation has previously been implicated in the inability to grow InP QDs to large diameters.[14,47] Thus far, water has been identified as the most likely primary source of oxygen atoms involved in phosphate formation.[44,48] Chaudret and co-workers characterized the amorphous surface oxide layer that is produced by the concurrent oxidation through a combination of XPS, IR, and SSNMR spectroscopy.[11]

**C**-InP was synthesized following a literature procedure in which $P(SiMe_3)_3$ was injected into a 300 °C 1-octadecene (ODE) bath of indium myristate and excess myristic acid.[49] The resulting particles have a lowest-energy electronic transition (LEET) at 530 nm and weak emission features comprised of a peak at 579 nm and a broad red-shifted shoulder that corresponds to the band edge and radiative surface defect emission, respectively. The normalized PL spectrum is shown in Figure S6 and corresponds to a PL QY of <1%.

In the second synthesis, atomically precise $In_{37}P_{20}(O_2CR)_{51}$ magic-sized clusters (MSCs) were used as single-source precursors.[41,50] Carboxylate-capped InP MSCs can be purified to remove any freely diffusing carboxylic acid, ensuring that the reaction solution is a homogeneous mixture of only the MSC. We found this to be an appealing choice for this study because the removal of acidic protons would ideally prevent decarboxylative coupling and aqueous byproducts. Hereafter, the QDs derived from InP MSCs are termed **M**-InP.

The production of **M**-InP requires two steps, the first step being the synthesis and isolation of $In_{37}P_{20}(O_2CR)_{51}$. This can be done by following the conditions to make **C**-InP QDs as described above but dropping the injection/growth temperature to 100 °C and performing the reaction in toluene.[41] The MSCs were purified through GPC and analyzed by $^1$H NMR spectroscopy to ensure the removal of excess acid (Figure S7). At this point, a portion of MSCs, which exist in the form of a waxy solid, can be dissolved in ODE and injected into a 300 °C solution of ODE. Depending on the concentration of MSCs in the growth solution, the particle size can be modified.[41] In this instance, a 60 mg injection of MSC produced particles with a LEET at 555 nm and emission features similar to those of **C**-InP with the band edge emission at 591 nm (Figure 3 and


DOI: 10.1021/acs.chemmater.8b02590
Chem. Mater. 2018, 30, 6377−6388

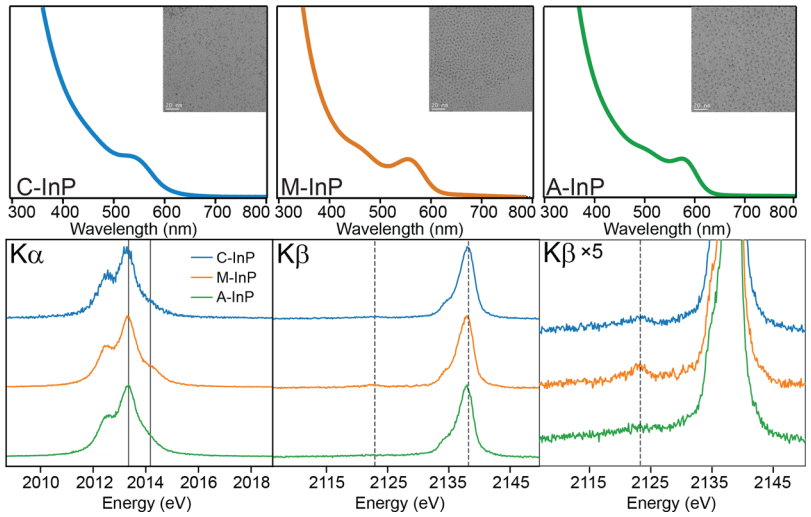


**Figure 3.** Final absorbance traces (top) of **C**-InP, **M**-InP, and **A**-InP with TEM image insets (20 nm scale bar) of purified material. P K$\alpha$ and K$\beta$ XES spectra (bottom) for the InP QD samples where solid vertical lines in the K$\alpha$ spectra indicate the InP component (2013.59 eV) and the identified phosphate component (2014.41 eV). In the K$\beta$ spectra, dashed lines indicate the K$\beta'$ peak of phosphate (2123.5 eV) and the K$\beta_{1,3}$ peak of bulk InP (2138.6 eV).

**Table 2. Phosphorus Speciation As Determined by Linear Combination Fitting to K$\alpha$ XES Spectra**[a]

| sample | reduced (%) | oxidized (%) | estimated uncertainty (%) | reduced K$\alpha_1$ energy (eV) | oxidized K$\alpha_1$ energy (eV) | reduced $\chi^2$ |
|---|---|---|---|---|---|---|
| **C**-InP | 89 | 11 | ±3 | 2013.54 | 2014.40 | 1.15 |
| **M**-InP | 84 | 16 | ±2 | 2013.57 | 2014.50 | 1.17 |
| **A**-InP | 83 | 17 | ±4 | 2013.59 | 2014.29 | 1.32 |
| **C**/ZnS | 51 | 49 | ±5 | 2013.57 | 2014.42 | 1.32 |
| **M**/ZnS | 62 | 38 | ±4 | 2013.55 | 2014.44 | 1.18 |
| **A**/ZnS | 57 | 43 | ±5 | 2013.58 | 2014.42 | 1.12 |
| **C**/ZnSe | 14 | 86 | ±9 | 2013.55 | 2014.32 | 1.02 |
| **M**/ZnSe | 16 | 84 | ±5 | 2013.53 | 2014.41 | 1.24 |
| **A**/ZnSe | 51 | 49 | ±5 | 2013.58 | 2014.45 | 1.06 |

[a]For the InP- and ZnS-shelled samples, the K$\alpha$1 energy positions from two-component fitting are reported. For the ZnSe-shelled samples, the K$\alpha$1 energy positions of the reduced and oxidized components are reported from three-component fitting.

Figure S6). The advantages of using this two-step route over traditional indium/phosphorus monomer nucleation are twofold in that the synthesis can be performed more reproducibly with a homogeneous precursor and the monodispersity of the resulting sample ensemble is improved. TEM images of **M**-InP QDs show this with more ordered packing due to the more uniform particle morphologies.

In the final synthesis method, we examined InP QDs prepared from indium halides and aminophosphines in a primary amine solvent. Aminophosphines have been introduced as reliable phosphorus precursors for the synthesis of size-tunable InP QDs when paired with indium halides.[51] The reaction between metal halides and aminophosphines is driven by the dual role of aminophosphines as a phosphorus source and a reducing agent.[19,52] More importantly for the work presented here, the aminophosphine synthesis does not involve any oxygen-containing reagents, eliminating the possibility of oxidation via reagent decomposition products. Hereafter, InP QDs synthesized with an aminophosphine P source will be termed **A**-InP.

The aminophosphine-based InP QD synthesis diverges from indium carboxylate/silylphosphine chemistry in that the solvent, a primary amine, is coordinating and so acts as a solvent and ligand and even plays a role in the precursor conversion reactions. Furthermore, Zn(II) was added to the precursor mixture prior to particle nucleation and has been observed to improve the resulting particle crystallinity and monodispersity. Further details can be found in the Experimental Section, but briefly, zinc chloride and indium chloride were heated to 180 °C in oleylamine followed by injection of tris(diethylamino)phosphine. The final **A**-InP particles have a LEET at 573 nm and an emission peak at 618 nm (3% PL QY) shown in Figure 3 and Figure S6. Replacing carboxylates as surface ligands with chlorides and amines also impacts particle morphology by preferentially binding to the (111) face as seen by the tetrahedral shape of the resulting particles.[14]

K$\alpha$ XES measurements were used to measure phosphorus speciation as described in the Experimental Section. The P K$\alpha$ emission spectra of **C**-, **M**-, and **A**-InP QDs are shown in Figure 3 with corresponding peak positions and speciation percentages summarized in Table 2. The lower-energy component is described as "reduced", and the higher-energy component is described as "oxidized". We attribute the 11% oxidized component measured in **C**-InP to the previously characterized ketonization reaction that occurs during particle growth, which is supported by the two phosphorus resonances in the $^{31}$P SSNMR spectrum (Figure 4a). At elevated temperatures, the excess acid undergoes decarboxylative coupling in which a ketone, carbon dioxide, and water are


DOI: 10.1021/acs.chemmater.8b02590
Chem. Mater. 2018, 30, 6377−6388

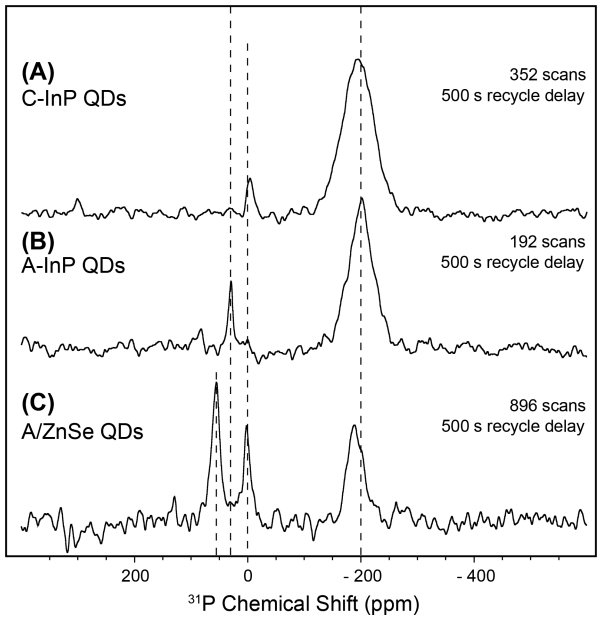


**Figure 4.** $^{31}$P SSNMR spectra of (A) **C**-InP QDs, (B) **A**-InP QDs, and (C) **A**/ZnSe QDs. Dashed lines are to guide the eye to −200 ppm (phosphide resonance), 0 ppm (phosphate resonance), 30 ppm (phosphonium salt resonance), and 55 ppm (TOPO resonance).

products. Our initial expectation from the **M**-InP was to circumvent water formation through the removal of acid [$^1$H NMR (Figure S7)]. As one can see from the 16% oxidized component of **M**-InP, this process was difficult to avoid. A solution $^{13}$C NMR spectrum of the **M**-InP QDs before purification shows an apparent peak in the expected region for a ketone carbon at 210 ppm (Figure S8); formation of ketone in the synthesis would be accompanied by the formation of water. There is a notable lack of an acidic proton in the $^1$H NMR spectrum of the initial MSCs, suggesting no free carboxylic acid is present prior to synthesis. Furthermore, the P K$\alpha$ emission spectrum of the stock MSCs shows that the starting material was not oxidized, which agrees with the single-crystal structure that is fully saturated with surface indium carboxylates (Figure S9).[50] However, we hypothesize that in the case of long-chain carboxylate ligands, carboxylic acid is difficult to remove due to hydrogen bonding interactions and entanglement of the aliphatic side chains with the carboxylate ligand shell.

Unexpectedly, we measured a 17% oxidized component in the **A**-InP QDs, a synthesis lacking any oxygen-containing precursors. The K$\alpha_1$ energy position of the oxidized population was notably lower than the component near 2014.41 eV identified above as phosphate, which led us to investigate further. P K$\beta$ XES can be used for exactly this question of ligand identity. The strong K$\beta'$ satellite feature at 2123.5 eV in the phosphate reference standard serves as a fingerprint of the presence of P−O bonds. P K$\beta$ spectra of **C**-, **M**-, and **A**-InP QDs are shown in Figure 3. The **C**-InP and **M**-InP show clear peaks at the phosphate energy position, in qualitative agreement with their relative proportion of oxidized component (11 and 16%, respectively). In contrast, the absence of the K$\beta'$ feature in the **A**-InP spectrum implies that the 17% oxidized component is not due to phosphate.

To investigate the identity of this component, we utilized XPS and solution $^{31}$P NMR spectroscopy to aid in the detection of potential reaction byproducts. Following multiple rounds of precipitation and GPC purification, we initially found that the solution $^{31}$P NMR spectrum of the stock solution contained no detectable resonances. Over the period of several weeks of storage in a nitrogen atmosphere glovebox, however, the solution $^{31}$P NMR spectrum revealed P-containing impurities at 80 and 30 ppm (Figure S12). The peak at 80 ppm lies in the region of transaminated species produced during this reaction that likely exist in equilibrium with phosphonium salt byproducts.[19,52] Phosphonium salts, $P(NHR)_4Cl$ in which R is an oleyl group, are the dominant reaction byproducts, forming 3 equiv for every InP unit, and have been previously identified in the $^{31}$P NMR spectrum to have a peak at 29 ppm. Although alternative routes to remove P-containing impurities exist (ligand exchange with thiols has met with success), subjecting the InP particle surface to further modification was not an ideal pathway with the goal of probing the surface defects intrinsic to the synthesis. The direct excitation the $^{31}$P SSNMR spectrum identified that there was a mixed environment of core InP, 91%, centered at −200 ppm and phosphonium salt, 9%, at 30 ppm with a notable absence of a signal at 0 ppm that would correspond to surface phosphate species (Figure 4b). The $P_{2p}$ XPS spectrum shown in Figure S11 further supports the identification of a mixed phosphide/phosphonium environment when compared to the peak position of a commercial phosphonium salt [aminotris-(dimethylamino)phosphonium chloride]. Lastly, we measured the P K$\alpha$ XES spectrum of the commercial phosphonium salt and observed a K$\alpha_1$ energy position at 2014.35 eV, which agrees well with the shift of the K$\alpha_1$ position to a lower energy for the **A**-InP sample. Taken together, this evidence supports the conclusion that the 17% oxidized component is a result of electrostatically interacting phosphonium impurities and the **A**-InP particle surface can be considered unsullied $P^{3-}$.

As demonstrated by the P K$\alpha$ emission spectra of InP QDs formed in the presence of carboxylate groups (**C** and **M** samples), ketonization is difficult to prevent, even following attempts to remove excess acid in the case of MSC precursors. Alternatively, utilizing aminophosphines effectively reduces the level of *in situ* oxidation while also minimizing the cost and hazard of the phosphorus precursor. Progress has been made toward other oxide-free syntheses in which InP is formed by heating indium carboxylates and $P(SiMe_3)_3$ in a 1.8 bar $H_2$ atmosphere.[17] The authors conclude that $H_2$ molecules are activated at the QD surface and yield P−H bonds that protect the surface through the concurrent water-forming condensation reactions. At this point, oxidative defect-free surfaces are accessible if a synthesis is being performed under $H_2$ or utilizing aminophosphines with indium halides, while offering different options for surface chemistry or particle morphologies. The general consensus in the field of InP QD chemistry is that the presence of surface phosphorus−oxygen bonds will detrimentally impact subsequent shell growth. We extend the characterization of InP QD oxidation through the addition of ZnE (E = S or Se) shells to gauge the effect further chemical transformations may have on the optical properties and oxidized populations of the InP samples.

**Impact of Oxidative Surface Species on Optical Properties.** We chose to examine the resulting properties of the series of **C**-, **M**-, and **A**-InP shelled with either a thin ZnS shell or a thick ZnSe shell. With regard to the ZnS shell, we refer back to the work Chaudret and co-workers performed in characterizing the InP−ZnS interface.[12] ZnS was grown by the


DOI: 10.1021/acs.chemmater.8b02590
Chem. Mater. 2018, 30, 6377−6388

successive ion layer adsorption and reaction (SILAR) approach in which zinc carboxylate and sulfur powder were added separately at elevated temperatures to drive reaction with the InP surface and prevent nucleation of ZnS nanoparticles.[43] Through extensive optimization, thin ZnS shells (<2 nm) have been able to increase the QYs of InP QDs to 60−70%. The Chaudret group found that InP is even further oxidized during shell growth because of a series of side reactions. First, elemental sulfur has been observed to form hydrogen sulfide through activation by the solvent, ODE.[53] $H_2S$ then reacts with zinc carboxylate to form carboxylic acids that promote ketonization and water production as seen in the initial InP core syntheses (**C**-InP). They found that the oxidized percentage of phosphorus in the core InP increased from 8 to 21% following shell growth. This approach to ZnS shell growth was selected to compare the impact of an established oxidation chemistry across the series of InP QDs.

The second comparison on which we focus is the growth of a thick (>5 nm) ZnSe shell. In addition to minimizing the surface defects to improve the core−shell interface, selecting materials with similar lattice constants aids in reducing strain. ZnSe has a 3.4% lattice mismatch with InP, which is smaller than that for ZnS at 7.7%, and thus may improve the optical properties of InP. Recently, thicker ZnSe shells have been reported in the literature to suppress the single-dot PL intermittency of InP QDs associated with nonradiative Auger processes, with QYs reaching 60%.[42,54] While the thick shell effectively cuts off interaction of carriers with the environment, the compressive strain induced upon the core nanoparticle can often lead to further lattice strain-related defects.[55] Some of the detrimental effects of thick shells have been offset by alloying, particularly at the interface, or by stacking materials with a gradient lattice, as observed in chalcogenide-based materials.[56−58]

Following purification by GPC, solutions of **C**-, **M**-, and **A**-InP were dissolved in either ODE or squalane for shell growth. Rather than optimize conditions for maximum QYs, we emphasized the comparison across initial InP syntheses by matching the concentration of the InP samples by standardizing the absorption at 310 nm across preshelled solutions to add the same amount of Zn and chalcogenide precursors. It should be noted that the particles are not precisely the same size (TEM and $\lambda_{max}$), in addition to particle polydispersity, which may contribute to differences among the observed shell thicknesses. A summary of particle characterization for this series of InP/ZnE QDs, including optical peak positions, compositions, particle sizes, and powder diffraction patterns, can be found in Table S3 and Figure S5.

ZnS shells were grown following a literature procedure in which zinc myristate and sulfur powder were added individually over 10 min intervals to InP QDs at elevated temperatures. This layer-by-layer approach was performed a second time for an intended two-monolayer ZnS shell. The resulting InP/ZnS particles exhibit a minor blue-shift in their features that we attribute to etching by $H_2S$ produced in the synthesis (Figure 5). The measured PL QYs and emission line widths for **C**/ZnS, **M**/ZnS, and **A**/ZnS were 7% (66 nm), 28% (56 nm), and 25% (69 nm), respectively. Comparatively, the emission line widths of highly optimized core−shell InP syntheses are 40−60 nm.[9]

The P K$\alpha$ emission spectra of the InP/ZnS samples demonstrate that each InP core was significantly oxidized (Figure 5). Peak positions, listed in Table 2, are in line with

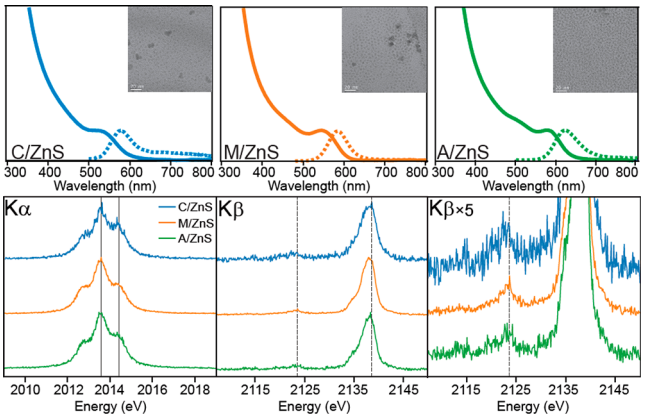


**Figure 5.** Final absorbance (solid) and PL (dashed) trace **C**/ZnS, **M**/ZnS, and **A**/ZnS with TEM image insets (20 nm scale bar) of purified material (top). P K$\alpha$ and K$\beta$ XES spectra (bottom) for the InP/ZnS samples where solid vertical lines in the K$\alpha$ spectra indicate the InP component (2013.59 eV) and the identified phosphate component (2014.41 eV). In the K$\beta$ spectra, dashed lines indicate the K$\beta'$ peak of phosphate (2123.5 eV) and the K$\beta_{1,3}$ peak of bulk InP (2138.6 eV).

our identified phosphate and phosphide components and show that the phosphate population for all samples increased to a range of 38−49%. The P K$\beta$ spectrum supports the identification of the oxidized component as phosphate, with strong K$\beta'$ peaks at 2123.5 eV (Figure 5). From previous reports of a shell growth-coupled oxidation event, we expected a substantial increase in the level of phosphorus oxidation. Surprisingly, the extent of phosphorus oxidation is apparently not dependent on the initial InP surface environment. Along those lines, it is difficult to correlate the extent of phosphorus oxidation with the optical properties because in each case a majority of the surface phosphorus was converted to phosphates. The important conclusion from this series of samples is that even when starting with an ideally oxidative defect-free surface, adventitious side reactions during shell growth will still significantly impact the InP surface and thus the core−shell interface.

With regard to InP/ZnSe, chemists have postulated that incomplete blinking suppression and low quantum yields (40−60%) originate from point defects at the core−shell interface, which was a reason to study these samples. As seen with ZnS shell growth, InP QD solutions were matched in concentration across **C**, **M**, and **A** to reliably compare across the three. Again, utilizing a SILAR approach, zinc myristate and trioctylphosphine-selenide (TOP-Se) were added to InP QDs at elevated temperatures at varying time intervals (see the Experimental Section for specific details). Two distinct features arise in the absorbance spectra, one of which is a significant increase in higher-energy absorbance due to the thick ZnSe shell. Second, the LEET experiences a red-shift due to the near overlap of the InP and ZnSe conduction band edges (Figure 6). The emission line widths range from 59 to 84 nm, with the **M**-InP giving the narrowest line width (59 nm) likely due to the improved monodispersity of the starting InP cores.

Compared to those of the InP/ZnS samples, the PL QYs of these unoptimized syntheses were slightly greater with a maximum of 44% for **M**/ZnSe and 10 and 30% for **C**/ZnSe and **A**/ZnSe, respectively. At least in the case of **C**/ZnSe, there was a mixture of thick-shelled particles and what could be partially shelled or unshelled InP QDs that limit the measured quantum yield (Figure 6). For a majority of the **C**/ZnSe and


DOI: 10.1021/acs.chemmater.8b02590
Chem. Mater. 2018, 30, 6377−6388

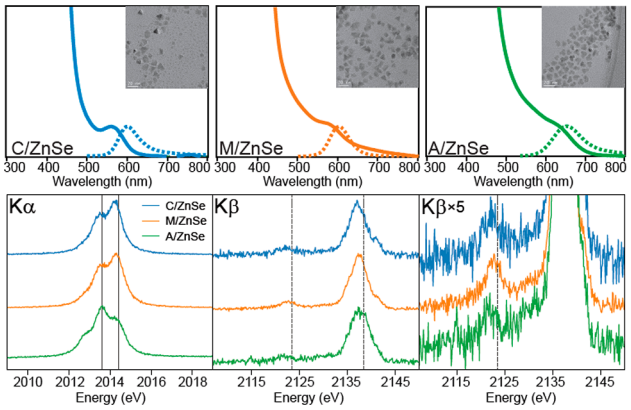


**Figure 6.** Final absorbance (solid) and PL (dashed) trace of **C**/ZnSe, **M**/ZnSe, and **A**/ZnSe with TEM image insets (20 nm scale bar) of purified material (top). P K$\alpha$ and K$\beta$ XES (bottom) spectra for the InP/ZnSe samples, where solid vertical lines in the K$\alpha$ spectra indicate the InP component (2013.59 eV) and the identified phosphate component (2014.41 eV). In the K$\beta$ spectra, dashed lines indicate the K$\beta'$ peak of phosphate (2123.5 eV) and the K$\beta_{1,3}$ peak of bulk InP (2138.6 eV).

**M**/ZnSe, the morphology of the shelled particles was tetrahedral while the **A**/ZnSe appeared to shell less uniformly and typically looked bulbous, suggesting shell nucleation occurred separately at each vertex of the InP tetrahedron as opposed to conformal shell deposition on the more spherical cores observed in **C** and **M**. Shell uniformity will also play a role in optimizing emissive properties due to the detrimental impact of structural defects. Furthermore, because of the substantial shell thickness, XPS analysis of the InP/ZnSe revealed only the phosphate peak, most likely because photoelectrons generated in the core phosphide have a lower probability of escaping (Figure S12). In this context, XPS becomes an imprecise and unreliable technique.

The P K$\alpha$ emission spectra of the InP/ZnSe, shown in Figure 6, were distinctive in that the peak positions from two-component fitting did not overlap with our identified phosphide and phosphate components. The energies of the oxidized K$\alpha_1$ peaks were decreased, and the energies of the K$\alpha_1$ peaks were increased (Table S4). These shifts, combined with the higher reduced $\chi^2$ statistic of the **A**/ZnSe and **M**/ZnSe fits, suggest that the two-component fitting procedure does not sufficiently explain the observed spectra. Furthermore, we observed several differences in the K$\beta$ emission spectra from typical InP such as the shift of the K$\beta_{1,3}$ peak to lower energies and a pronounced shoulder at 2140.5 eV (Figure 6).

To reconcile these clear changes in the K$\alpha$ and K$\beta$ spectra for the ZnSe-shelled samples, we considered the possibility of a third significant phosphorus species present in the sample. Fortunately, the main decomposition product of TOP-Se has been previously identified as trioctylphosphine oxide (TOPO) through precursor evolution studies of cadmium chalcogenide nanocrystals.[59,60] The K$\beta$ emission spectrum of TOPO (shown in Figure 1) qualitatively matched the distinctive features observed in the InP/ZnSe samples. Although sample purification focused on the removal of excess ligands and byproducts, complete removal is often complicated because of the entanglement of long-chain hydrocarbons and in this case by weak binding of the TOPO to the particle surface. Thus, to evaluate the reduced and oxidized populations excluding the TOPO component, the K$\alpha$ spectra were fit with three P K$\alpha_{1,2}$ doublets as described in the Experimental Section. This procedure results in improved fits for the **A**/ZnSe and **M**/ZnSe samples (Figure S13) and improved K$\alpha_1$ energy positions for all three samples (Table S5). Our analysis was further supported by the $^{31}$P SSNMR spectrum of the **A**/ZnSe sample in which three populations of phosphorus are measured: phosphide at −200 ppm, phosphate at 0 ppm, and TOPO at 55 ppm. Their integrated areas agree qualitatively with the three-component fitting results (F6). The presence of a significant phosphate species in each of these samples also agrees qualitatively with the K$\beta$ spectra, each of which has a significant phosphate K$\beta'$ peak near 2123.5 eV, much stronger in proportion than the spectral features exhibited in the TOPO spectrum.

X-ray emission spectra of InP/ZnSe samples show very highly oxidized components. In the case of **A**/ZnSe, roughly 51% of the phosphorus remains as phosphide while a mere ∼15% of the phosphide component in **C**/ZnSe or **M**/ZnSe was retained. We estimated that the core InP particles would have roughly 55−70% of the total phosphorus exposed to the surface; thus, while the pathway of oxidation during ZnSe shell growth is unknown, it is reasonable that nearly all surface sites are oxidized. Additionally, we would not expect oxidative defects to penetrate beyond the surface of the InP core, so we suggest that anion diffusion occurs during shell growth (in the case of thick shells) that allows core phosphides to migrate to the surface of the shell. Evidence supporting this proposed anion diffusion mechanism was presented by Rosenthal et al.; the energy dispersive X-ray chemical maps of InP/ZnSe particles demonstrate alloying of In/P atoms into the Zn/Se shell.[54] They hypothesized that alloying helps mitigate the increasing strain induced by the growth of a thick shell.

Our goal to examine the correlation between surface oxidation and luminescence properties in the InP/ZnSe samples was similarly obstructed by excessive oxidation that prevented a careful analysis of these key factors. As with the InP/ZnS particles, the core−shell interface is thoroughly oxidized regardless of the defect-free surface of the starting materials (i.e., **A**-InP). These results emphasize the importance of critically examining the chemistry occurring after the InP core growth phase, especially when rigorous care is taken to improve the quality of the core particles. There has been growing interest in addressing the issue of introducing oxidative defects during shell growth. For example, Jeong et al. targeted the growth of a ZnS shell in the absence of acid-containing precursors and reported a phosphate-free interface, but the PL QYs of these samples still plateaued at 60%.[14] If indeed the particles experienced no oxidation through core/shell growth, which was assessed via XPS, nonradiative recombination defect sites likely still formed as a combined result of compressive strain because of the growth of a >5 nm shell and the lattice mismatch between InP and ZnS.

## CONCLUSIONS

Using a recently developed benchtop X-ray emission spectrometer, we have demonstrated the viability of phosphorus K$\alpha$ XES measurements as a quantitative analytical tool for characterizing the extent of oxidation in InP quantum dots through a comparative analysis with $^{31}$P SSNMR spectroscopy. With the aid of measurements of the valence-to-core P K$\beta$ emission using the same spectrometer, we were able to identify the presence of phosphate species and


DOI: 10.1021/acs.chemmater.8b02590
Chem. Mater. 2018, 30, 6377−6388

phosphine/phosphonium salt byproducts, which were also confirmed by $^{31}$P SSNMR. XES measurements gave us the capability to rapidly measure a large volume of samples with excellent resolution from only a few milligrams of deposited material. This demonstration strongly suggests a future in which benchtop XES plays a role in the routine analysis of phosphorus compounds and materials.

We examined the impact of phosphorus oxidation on InP optical properties by measuring surface phosphorus oxidation as a function of synthetic method and shelling strategy. The high degree of oxidation in the shelled compounds limits a careful interpretation of the correlation between QY and oxidized P, while being further complicated by various other synthetic factors. In this regard, the use of ultrafast spectroscopy and high-resolution electron microscopy may aid in elucidating a more apparent relationship. While there are routes to achieving a phosphate-free surface, these result in the specific ligation environment and particle morphology associated with indium halides and aminophosphine precursors. To expand upon the available options, it may serve the field to develop a deeper understanding of the mechanism involving fluoride etching to address surface defects on QD surfaces[61,62] and develop new chemical methods for removing phosphate defects. Side reactions occurring during shell growth further oxidize the interface to the extent that the initial condition of the core surface is inconsequential. Current industry patents cite the usage of the same precursors examined in this study, implicating the presence of oxidized surfaces and rationalizing the lower than expected PL QYs.[6] This strongly motivates a push toward designing shelling syntheses involving innocent precursors in an effort to minimize interfacial defect sites and optimizing conditions to prevent significant diffusion of phosphorus from the QD core.

## ■ ASSOCIATED CONTENT

### Supporting Information

The Supporting Information is available free of charge on the ACS Publications website at DOI: 10.1021/acs.chemmater.8b02590.

Additional details regarding X-ray emission spectral fitting and QD characterization (PDF)

## ■ AUTHOR INFORMATION


### Corresponding Authors

*E-mail: cossairt@chem.washington.edu.
*E-mail: seidler@uw.edu.

### ORCID

Jennifer L. Stein: 0000-0002-6553-5116
Amrit Venkatesh: 0000-0001-5319-9269
Aaron J. Rossini: 0000-0002-1679-9203
Gerald T. Seidler: 0000-0001-6738-7930
Brandi M. Cossairt: 0000-0002-9891-3259


### Author Contributions

J.L.S. and W.M.H. contributed equally to this work.

### Notes

The authors declare no competing financial interest.

## ■ ACKNOWLEDGMENTS

This research (B.M.C. and J.L.S.) was partially supported by the U.S. National Science Foundation through the University of Washington Molecular Engineering Materials Center, a Materials Research Science and Engineering Center (Grant DMR-1719797). This work (W.M.H. and G.T.S.) was partially supported by the Joint Plasma Physics Program of the National Science Foundation and the U.S. Department of Energy (DOE) under Grant DE-SC0016251. A.J.R. and A.V. were supported by the DOE, Office of Science, Basic Energy Sciences, Materials Science and Engineering Division. The Ames Laboratory is operated for the DOE by Iowa State University under Contract DE-AC02-07CH11358. Part of this work was conducted at the Molecular Analysis Facility, a National Nanotechnology Coordinated Infrastructure site at the University of Washington, which is supported in part by the National Science Foundation (Grant ECC-1542101), the University of Washington, the Molecular Engineering & Sciences Institute, the Clean Energy Institute, and the National Institutes of Health.

## ■ ABBREVIATIONS

QD, quantum dot; PL, photoluminescence; QY, quantum yield; MAS, magic angle spinning; SSNMR, solid state nuclear magnetic resonance; XES, X-ray emission spectroscopy; XPS, X-ray photoelectron spectroscopy; ICP-OES, inductively coupled plasma optical emission spectroscopy; LEET, lowest-energy electronic transition; XRD, X-ray diffraction; TEM, transmission electron microscopy; MSC, magic-sized cluster; ODE, 1-octadecene; GPC, gel permeation chromatography.

## ■ REFERENCES


(1) Chopra, S. S.; Theis, T. L. Comparative Cradle-to-Gate Energy Assessment of Indium Phosphide and Cadmium Selenide Quantum Dot Displays. *Environ. Sci.: Nano* **2017**, *4*, 244−254.

(2) Shirasaki, Y.; Supran, G. J.; Bawendi, M. G.; Bulovic, V. Emergence of Colloidal Quantum-Dot Light-Emitting Technologies. *Nat. Photonics* **2013**, *7*, 13−23.

(3) Supran, G. J.; Shirasaki, Y.; Song, K. W.; Caruge, J.-M.; Kazlas, P. T.; Coe-Sullivan, S.; Andrew, T. L.; Bawendi, M. G.; Bulović, V. QLEDs for Displays and Solid-State Lighting. *MRS Bull.* **2013**, *38*, 703−711.

(4) Steckel, J. S.; Ho, J.; Hamilton, C.; Xi, J.; Breen, C.; Liu, W.; Allen, P.; Coe-Sullivan, S. Quantum Dots: The Ultimate down-Conversion Material for LCD Displays. *J. Soc. Inf. Disp.* **2015**, *23*, 294−305.

(5) Anc, M. J.; Pickett, N. L.; Gresty, N. C.; Harris, J. A.; Mishra, K. C. Progress in Non-Cd Quantum Dot Development for Lighting Applications. *ECS J. Solid State Sci. Technol.* **2013**, *2*, R3071−R3082.

(6) Jun, S. A.; Jang, E. J.; Kwon, S. K.; Kim, T. H.; Lee, W. J. Semiconductor Nanocrystal, and Method of Preparing the Same. US20140117292A1, 2014.

(7) Kim, S.; Kim, T.; Kang, M.; Kwak, S. K.; Yoo, T. W.; Park, L. S.; Yang, I.; Hwang, S.; Lee, J. E.; Kim, S. K.; et al. Highly Luminescent InP/GaP/ZnS Nanocrystals and Their Application to White Light-Emitting Diodes. *J. Am. Chem. Soc.* **2012**, *134*, 3804−3809.

(8) Lim, J.; Bae, W. K.; Lee, D.; Nam, M. K.; Jung, J.; Lee, C.; Char, K.; Lee, S. InP@ZnSeS, Core@Composition Gradient Shell Quantum Dots with Enhanced Stability. *Chem. Mater.* **2011**, *23*, 4459−4463.

(9) Tamang, S.; Lincheneau, C.; Hermans, Y.; Jeong, S.; Reiss, P. Chemistry of InP Nanocrystal Syntheses. *Chem. Mater.* **2016**, *28*, 2491−2506.

(10) Jasinski, J.; Leppert, V. J.; Lam, S.-T.; Gibson, G. A.; Nauka, K.; Yang, C. C.; Zhou, Z.-L. Rapid Oxidation of InP Nanoparticles in Air. *Solid State Commun.* **2007**, *141*, 624−627.

(11) Cros-Gagneux, A.; Delpech, F.; Nayral, C.; Cornejo, A.; Coppel, Y.; Chaudret, B. Surface Chemistry of InP Quantum Dots: A Comprehensive Study. *J. Am. Chem. Soc.* **2010**, *132*, 18147−18157.

(12) Virieux, H.; Le Troedec, M.; Cros-Gagneux, A.; Ojo, W.-S.; Delpech, F.; Nayral, C.; Martinez, H.; Chaudret, B. InP/ZnS




DOI: 10.1021/acs.chemmater.8b02590
*Chem. Mater.* 2018, 30, 6377−6388

Nanocrystals: Coupling NMR and XPS for Fine Surface and Interface Description. *J. Am. Chem. Soc.* **2012**, *134*, 19701−19708.
(13) Ramasamy, P.; Kim, B.; Lee, M.-S.; Lee, J.-S. Beneficial Effects of Water in the Colloidal Synthesis of InP/ZnS Core−Shell Quantum Dots for Optoelectronic Applications. *Nanoscale* **2016**, *8*, 17159−17168.
(14) Kim, K.; Yoo, D.; Choi, H.; Tamang, S.; Ko, J.-H.; Kim, S.; Kim, Y.-H.; Jeong, S. Halide−Amine Co-Passivated Indium Phosphide Colloidal Quantum Dots in Tetrahedral Shape. *Angew. Chem., Int. Ed.* **2016**, *55*, 3714−3718.
(15) Gary, D. C.; Cossairt, B. M. Role of Acid in Precursor Conversion During InP Quantum Dot Synthesis. *Chem. Mater.* **2013**, *25*, 2463−2469.
(16) Xie, L.; Harris, D. K.; Bawendi, M. G.; Jensen, K. F. Effect of Trace Water on the Growth of Indium Phosphide Quantum Dots. *Chem. Mater.* **2015**, *27*, 5058−5063.
(17) Baquero, E. A.; Virieux, H.; Swain, R. A.; Gillet, A.; Cros-Gagneux, A.; Coppel, Y.; Chaudret, B.; Nayral, C.; Delpech, F. Synthesis of Oxide-Free InP Quantum Dots: Surface Control and $H_2$-Assisted Growth. *Chem. Mater.* **2017**, *29*, 9623−9627.
(18) Xi, L.; Cho, D.-Y.; Besmehn, A.; Duchamp, M.; Grützmacher, D.; Lam, Y. M.; Kardynał, B. E. Effect of Zinc Incorporation on the Performance of Red Light Emitting InP Core Nanocrystals. *Inorg. Chem.* **2016**, *55*, 8381−8386.
(19) Buffard, A.; Dreyfuss, S.; Nadal, B.; Heuclin, H.; Xu, X.; Patriarche, G.; Mézailles, N.; Dubertret, B. Mechanistic Insight and Optimization of InP Nanocrystals Synthesized with Aminophosphines. *Chem. Mater.* **2016**, *28*, 5925−5934.
(20) Berends, A. C.; van der Stam, W.; Hofmann, J. P.; Bladt, E.; Meeldijk, J. D.; Bals, S.; de Mello Donega, C. Interplay between Surface Chemistry, Precursor Reactivity, and Temperature Determines Outcome of ZnS Shelling Reactions on $CuInS_2$ Nanocrystals. *Chem. Mater.* **2018**, *30*, 2400−2413.
(21) Holden, W. M.; Hoidn, O. R.; Ditter, A. S.; Seidler, G. T.; Kas, J.; Stein, J. L.; Cossairt, B. M.; Kozimor, S. A.; Guo, J.; Ye, Y.; et al. A Compact Dispersive Refocusing Rowland Circle X-Ray Emission Spectrometer for Laboratory, Synchrotron, and XFEL Applications. *Rev. Sci. Instrum.* **2017**, *88*, 073904.
(22) Holden, W.; Seidler, G. T.; Cheah, S. Sulfur Speciation in Biochars by Very High Resolution Benchtop K$\alpha$ X-Ray Emission Spectroscopy. *J. Phys. Chem. A* **2018**, *122*, 5153−5161.
(23) Petric, M.; Kavčič, M. Chemical Speciation via X-Ray Emission Spectroscopy in the Tender X-Ray Range. *J. Anal. At. Spectrom.* **2016**, *31*, 450−457.
(24) Petric, M.; Bohinc, R.; Bučar, K.; Žitnik, M.; Szlachetko, J.; Kavčič, M. Chemical State Analysis of Phosphorus Performed by X-Ray Emission Spectroscopy. *Anal. Chem.* **2015**, *87*, 5632−5639.
(25) Alonso Mori, R.; Paris, E.; Giuli, G.; Eeckhout, S. G.; Kavčič, M.; Žitnik, M.; Bučar, K.; Pettersson, L. G. M.; Glatzel, P. Electronic Structure of Sulfur Studied by X-Ray Absorption and Emission Spectroscopy. *Anal. Chem.* **2009**, *81*, 6516−6525.
(26) Kavčič, M.; Petric, M.; Vogel-Mikuš, K. Chemical Speciation Using High Energy Resolution PIXE Spectroscopy in the Tender X-Ray Range. *Nucl. Instrum. Methods Phys. Res., Sect. B* **2018**, *417*, 65−69.
(27) Kavčič, M.; Karydas, A. G.; Zarkadas, C. Chemical State Analysis of Sulfur in Samples of Environmental Interest Using High Resolution Measurement of K$\alpha$ Diagram Line. *Nucl. Instrum. Methods Phys. Res., Sect. B* **2004**, *222*, 601−608.
(28) Pollock, C. J.; DeBeer, S. Insights into the Geometric and Electronic Structure of Transition Metal Centers from Valence-to-Core X-Ray Emission Spectroscopy. *Acc. Chem. Res.* **2015**, *48*, 2967−2975.
(29) Kowalska, J.; DeBeer, S. The Role of X-Ray Spectroscopy in Understanding the Geometric and Electronic Structure of Nitrogenase. *Biochim. Biophys. Acta, Mol. Cell Res.* **2015**, *1853*, 1406−1415.
(30) Pollock, C. J.; DeBeer, S. Valence-to-Core X-Ray Emission Spectroscopy: A Sensitive Probe of the Nature of a Bound Ligand. *J. Am. Chem. Soc.* **2011**, *133*, 5594−5601.
(31) Lancaster, K. M.; Roemelt, M.; Ettenhuber, P.; Hu, Y.; Ribbe, M. W.; Neese, F.; Bergmann, U.; DeBeer, S. X-Ray Emission Spectroscopy Evidences a Central Carbon in the Nitrogenase Iron-Molybdenum Cofactor. *Science* **2011**, *334*, 974−977.
(32) Mori, R. A.; Paris, E.; Giuli, G.; Eeckhout, S. G.; Kavčič, M.; Žitnik, M.; Bučar, K.; Pettersson, L. G. M.; Glatzel, P. Sulfur-Metal Orbital Hybridization in Sulfur-Bearing Compounds Studied by X-Ray Emission Spectroscopy. *Inorg. Chem.* **2010**, *49*, 6468−6473.
(33) Lee, N.; Petrenko, T.; Bergmann, U.; Neese, F.; DeBeer, S. Probing Valence Orbital Composition with Iron K$\beta$ X-Ray Emission Spectroscopy. *J. Am. Chem. Soc.* **2010**, *132*, 9715−9727.
(34) Bergmann, U.; Horne, C. R.; Collins, T. J.; Workman, J. M.; Cramer, S. P. Chemical Dependence of Interatomic X-Ray Transition Energies and Intensities − a Study of Mn K$\beta''$ and K$\beta$2,5 Spectra. *Chem. Phys. Lett.* **1999**, *302*, 119−124.
(35) Holden, W. M.; Hoidn, O. R.; Seidler, G. T. A Color X-Ray Camera for 2 − 6 KeV Using a Back-Illuminated Mass-Produced Complementary Metal Oxide Semiconductor Sensor. *Rev. Sci. Instrum.* **2018**, manuscript in press.
(36) Newville, M.; Stensitzki, T.; Allen, D. B.; Ingargiola, A. Lmfit: Non-Linear Least-Square Minimization And Curve-Fitting For Python. 2014.
(37) Glassy, B. A.; Cossairt, B. M. Ternary Synthesis of Colloidal Zn3P2 Quantum Dots. *Chem. Commun.* **2015**, *51*, 5283−5286.
(38) Shen, Y.; Gee, M. Y.; Tan, R.; Pellechia, P. J.; Greytak, A. B. Purification of Quantum Dots by Gel Permeation Chromatography and the Effect of Excess Ligands on Shell Growth and Ligand Exchange. *Chem. Mater.* **2013**, *25*, 2838−2848.
(39) Roberge, A.; Stein, J. L.; Shen, Y.; Cossairt, B. M.; Greytak, A. B. Purification and In Situ Ligand Exchange of Metal-Carboxylate-Treated Fluorescent InP Quantum Dots via Gel Permeation Chromatography. *J. Phys. Chem. Lett.* **2017**, *8*, 4055−4060.
(40) Stein, J. L.; Mader, E. A.; Cossairt, B. M. Luminescent InP Quantum Dots with Tunable Emission by Post-Synthetic Modification with Lewis Acids. *J. Phys. Chem. Lett.* **2016**, *7*, 1315−1320.
(41) Gary, D. C.; Terban, M. W.; Billinge, S. J. L.; Cossairt, B. M. Two-Step Nucleation and Growth of InP Quantum Dots via Magic-Sized Cluster Intermediates. *Chem. Mater.* **2015**, *27*, 1432−1441.
(42) Chandrasekaran, V.; Tessier, M. D.; Dupont, D.; Geiregat, P.; Hens, Z.; Brainis, E. Nearly Blinking-Free, High-Purity Single-Photon Emission by Colloidal InP/ZnSe Quantum Dots. *Nano Lett.* **2017**, *17*, 6104−6109.
(43) Xie, R.; Battaglia, D.; Peng, X. Colloidal InP Nanocrystals as Efficient Emitters Covering Blue to Near-Infrared. *J. Am. Chem. Soc.* **2007**, *129*, 15432−15433.
(44) Baquero, E. A.; Ojo, W.-S.; Coppel, Y.; Chaudret, B.; Urbaszek, B.; Nayral, C.; Delpech, F. Identifying Short Surface Ligands on Metal Phosphide Quantum Dots. *Phys. Chem. Chem. Phys.* **2016**, *18*, 17330−17334.
(45) Tomaselli, M.; Yarger, J. L.; Bruchez, M.; Havlin, R. H.; deGraw, D.; Pines, A.; Alivisatos, A. P. NMR Study of InP Quantum Dots: Surface Structure and Size Effects. *J. Chem. Phys.* **1999**, *110*, 8861−8864.
(46) Battaglia, D.; Peng, X. Formation of High Quality InP and InAs Nanocrystals in a Noncoordinating Solvent. *Nano Lett.* **2002**, *2*, 1027−1030.
(47) Ramasamy, P.; Ko, K.-J.; Kang, J.-W.; Lee, J.-S. Two-Step "Seed-Mediated" Synthetic Approach to Colloidal Indium Phosphide Quantum Dots with High-Purity Photo- and Electroluminescence. *Chem. Mater.* **2018**, *30*, 3643−3647.
(48) Cervilla, A.; Pérez-Pla, F.; Llopis, E.; Piles, M. Unusual Oxidation of Phosphines Employing Water as the Oxygen Atom Source and Tris(Benzene-1,2-Dithiolate)Molybdenum(VI) as the Oxidant. A Functional Molybdenum Hydroxylase Analogue System. *Inorg. Chem.* **2006**, *45*, 7357−7366.
(49) Gary, D. C.; Glassy, B. A.; Cossairt, B. M. Investigation of Indium Phosphide Quantum Dot Nucleation and Growth Utilizing Triarylsilylphosphine Precursors. *Chem. Mater.* **2014**, *26*, 1734−1744.


DOI: 10.1021/acs.chemmater.8b02590
*Chem. Mater.* 2018, 30, 6377−6388

(50) Gary, D. C.; Flowers, S. E.; Kaminsky, W.; Petrone, A.; Li, X.; Cossairt, B. M. Single-Crystal and Electronic Structure of a 1.3 Nm Indium Phosphide Nanocluster. *J. Am. Chem. Soc.* **2016**, *138*, 1510−1513.
(51) Tessier, M. D.; Dupont, D.; De Nolf, K.; De Roo, J.; Hens, Z. Economic and Size-Tunable Synthesis of InP/ZnE (E = S, Se) Colloidal Quantum Dots. *Chem. Mater.* **2015**, *27*, 4893−4898.
(52) Tessier, M. D.; De Nolf, K.; Dupont, D.; Sinnaeve, D.; De Roo, J.; Hens, Z. Aminophosphines: A Double Role in the Synthesis of Colloidal Indium Phosphide Quantum Dots. *J. Am. Chem. Soc.* **2016**, *138*, 5923−5929.
(53) Li, Z.; Ji, Y.; Xie, R.; Grisham, S. Y.; Peng, X. Correlation of CdS Nanocrystal Formation with Elemental Sulfur Activation and Its Implication in Synthetic Development. *J. Am. Chem. Soc.* **2011**, *133*, 17248−17256.
(54) Reid, K. R.; McBride, J. R.; Freymeyer, N. J.; Thal, L. B.; Rosenthal, S. J. Chemical Structure, Ensemble and Single-Particle Spectroscopy of Thick-Shell InP−ZnSe Quantum Dots. *Nano Lett.* **2018**, *18*, 709−716.
(55) Gong, K.; Kelley, D. F. Lattice Strain Limit for Uniform Shell Deposition in Zincblende CdSe/CdS Quantum Dots. *J. Phys. Chem. Lett.* **2015**, *6*, 1559−1562.
(56) Nasilowski, M.; Spinicelli, P.; Patriarche, G.; Dubertret, B. Gradient CdSe/CdS Quantum Dots with Room Temperature Biexciton Unity Quantum Yield. *Nano Lett.* **2015**, *15*, 3953−3958.
(57) Jeong, B. G.; Park, Y.-S.; Chang, J. H.; Cho, I.; Kim, J. K.; Kim, H.; Char, K.; Cho, J.; Klimov, V. I.; Park, P.; et al. Colloidal Spherical Quantum Wells with Near-Unity Photoluminescence Quantum Yield and Suppressed Blinking. *ACS Nano* **2016**, *10*, 9297−9305.
(58) Bae, W. K.; Padilha, L. A.; Park, Y.-S.; McDaniel, H.; Robel, I.; Pietryga, J. M.; Klimov, V. I. Controlled Alloying of the Core−Shell Interface in CdSe/CdS Quantum Dots for Suppression of Auger Recombination. *ACS Nano* **2013**, *7*, 3411−3419.
(59) Frenette, L. C.; Krauss, T. D. Uncovering Active Precursors in Colloidal Quantum Dot Synthesis. *Nat. Commun.* **2017**, *8*, 2082.
(60) Liu, H.; Owen, J. S.; Alivisatos, A. P. Mechanistic Study of Precursor Evolution in Colloidal Group II−VI Semiconductor Nanocrystal Synthesis. *J. Am. Chem. Soc.* **2007**, *129*, 305−312.
(61) Lovingood, D. D.; Strouse, G. F. Microwave Induced In-Situ Active Ion Etching of Growing InP Nanocrystals. *Nano Lett.* **2008**, *8*, 3394−3397.
(62) Siramdas, R.; McLaurin, E. J. InP Nanocrystals with Color-Tunable Luminescence by Microwave-Assisted Ionic-Liquid Etching. *Chem. Mater.* **2017**, *29*, 2101−2109.



DOI: 10.1021/acs.chemmater.8b02590
*Chem. Mater.* 2018, 30, 6377−6388